GEOCHEMISTRY

Extensive crystal fractionation of high-silica magmas revealed by K isotopes

Ze-Zhou Wang[1]*, Fang-Zhen Teng[1]*, Fu-Yuan Wu[2], Zhi-Chao Liu[3], Xiao-Chi Liu[2], Sheng-Ao Liu[4], Tian-Yi Huang[1]

Fractional crystallization plays a critical role in generating the differentiated continental crust on Earth. However, whether efficient crystal-melt separation can occur in viscous felsic magmas remains a long-standing debate because of the difficulty in discriminating between differentiated melts and complementary cumulates. Here, we found large (~1 per mil) potassium isotopic variation in 54 strongly peraluminous high-silica (silicon dioxide >70 weight %) leucogranites from the Himalayan orogen, with potassium isotopes correlated with trace elemental proxies (e.g., strontium, rubidium/strontium, and europium anomaly) for plagioclase crystallization. Quantitative modeling requires up to ~60 to 90% fractional crystallization to account for the progressively light potassium isotopic composition of the fractionated leucogranites, while plagioclase accumulation results in enrichment of heavy potassium isotopes in cumulate leucogranites. Our findings strongly support fractional crystallization of high-silica magmas and highlight the great potential of potassium isotopes in studying felsic magma differentiation.

INTRODUCTION

Magmatic differentiation induced by continuous crystal-melt segregation plays an important role in shifting the composition of Earth's continental crust from mafic to felsic (*1*, *2*). However, despite the well-constrained dynamics of crystal settling from mafic magmas (*3*), it remains debated whether—and, if so, how—efficient segregation of crystals occurs in silicic magmas (*4*–*12*), which solidify to form the major components (e.g., granites) of the upper continental crust (*13*). High-silica [>70 weight % (wt %) SiO_2] liquids are characterized by high viscosities and similar densities to the main crystallizing phases such as quartz and feldspar, meaning that fast and large-scale gravity-driven settling and accumulation of crystals are hard to achieve (*5*, *6*, *10*). Alternatively, compaction of crystal mush and hindered settling have been argued as probable mechanisms of separation of high-silica melts and complementary felsic cumulate residues (*4*, *5*, *12*). However, unlike mafic magmatic systems where numerous examples of cumulate textures have been observed [e.g., (*14*)], unequivocal petrological evidence for crystal accumulation in felsic rocks is elusive (*15*). This may be because either felsic cumulates are rare in the accessible parts of the continental crust (*16*, *17*) or the cumulates are not readily distinguishable from the differentiated high-silica melts possibly due to the trap of interstitial melts in crystal mushes, resulting in similar mineral assemblages and bulk chemical compositions between cumulates and fractionated melts (*4*, *15*). Furthermore, the subtle major elemental variations in evolved high-silica igneous rocks make it difficult to discriminate between strongly and weakly fractionated melts based on bulk rock chemistry such as SiO_2 and MgO (*18*), which are widely used in tracing the differentiation of mafic-intermediate magmas.

Potassium (K), with two stable isotopes (^{41}K and ^{39}K), is highly concentrated in high-silica magmas. The compatibility of K is opposite in plagioclase and K-feldspar (*19*), which are two ubiquitous and major phases in crystallizing assemblages of high-silica magmas. Thus, any change in the modes of plagioclase and K-feldspar will affect the geochemical behavior of K during fractional crystallization of high-silica magmas, leading to the nonsystematic variation in K concentration commonly observed in high-silica igneous rocks [e.g., (*18*, *20*, *21*)]. Recent studies revealed large K isotope fractionation among minerals in igneous rocks (*22*–*24*). In particular, plagioclase is significantly enriched in ^{41}K compared to other coexisting rock-forming minerals [e.g., K-feldspar, hornblende, and mica; (*23*, *24*)] due to the decrease in K—O bond length with (Na + Ca)/K in feldspars (*25*, *26*). Accordingly, systematic K isotopic variation might be expected in melts that experience different degrees of plagioclase crystallization. To date, only two studies reported limited K isotope fractionation during magmatic differentiation of basalts (*27*, *28*). This is consistent with the low concentrations of K in the major crystallization phases of mafic magmas (e.g., olivine and pyroxene), leaving the K isotopic system in melts undisturbed. By contrast, scarce data for high-silica granites suggest slightly more variable and lighter K isotopic compositions compared to mafic-intermediate rocks, which was not only previously ascribed to source heterogeneity (*29*) but may also result from the segregation of isotopically heavy feldspars (*28*).

To explore the potential of K isotopes in studying the magmatic differentiation of felsic magmas, we performed high-precision K isotopic analysis on a suite of well-characterized leucogranites from the Himalayan orogen (fig. S1). These leucogranites exhibit high-silica and strongly peraluminous characteristics of S-type granites (Fig. 1A and fig. S2) (*18*, *30*). Their parental melts formed via anatexis of granulite- to eclogite-facies metasediments with little evidence for either the presence of mafic rocks in their sources or mixing with mantle-derived or more juvenile mafic melts (*30*, *31*). Therefore, these leucogranites provide an excellent opportunity to investigate the magma chamber processes in an exclusive high-silica magmatic system. We found ~1 per mil (‰) K isotopic variation in the Himalayan leucogranite samples, which is most likely produced by plagioclase fractionation and accumulation during magmatic differentiation.

[1]Isotope Laboratory, Department of Earth and Space Sciences, University of Washington, Seattle, WA 98195, USA. [2]State Key Laboratory of Lithospheric Evolution, Institute of Geology and Geophysics, Chinese Academy of Sciences, Beijing 100029, China. [3]Guangdong Provincial Key Lab of Geodynamics and Geohazards, School of Earth Sciences and Engineering, Sun Yat-sen University, Guangzhou 510275, China. [4]State Key Laboratory of Geological Processes and Mineral Resources, China University of Geosciences, Beijing 100083, China.
*Corresponding author. Email: zzwang74@uw.edu (Z.-Z.W.); fteng@uw.edu (F.-Z.T.)

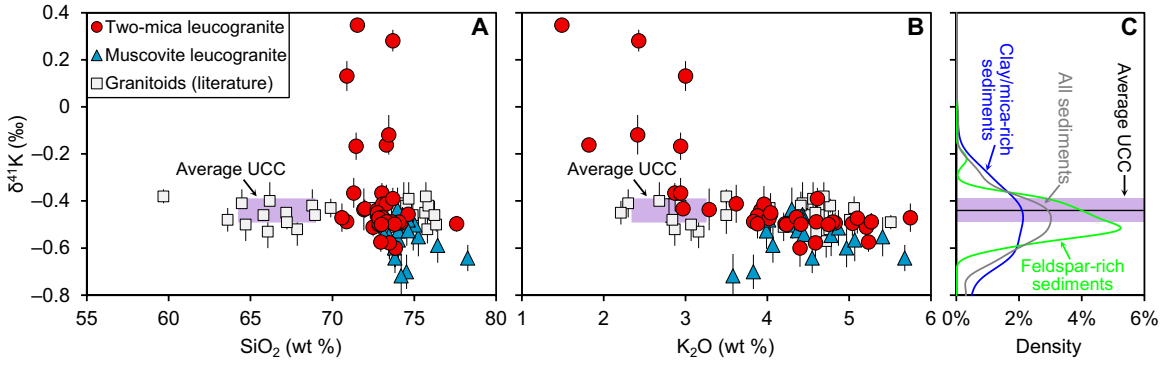

Fig. 1. Potassium isotopic compositions of the Himalayan leucogranites. (**A**) $\delta^{41}K$ versus SiO_2. (**B**) $\delta^{41}K$ versus K_2O. (**C**) Kernel density distributions of the $\delta^{41}K$ value for potential source lithologies of the Himalayan leucogranites [clay/mica-rich sediments (i.e., pelite, shale, clay, and mud): (*29*, *72*–*75*); feldspar-rich sediments (i.e., graywacke, sandstone, and siltstone): (*29*, *75*, *76*)]. Data for global granitoids from (*29*) are plotted for comparison in (A) and (B). The purple areas are the SiO_2 content (66.6 ± 2.4 wt %), K_2O content (2.80 ± 0.46 wt %), and $\delta^{41}K$ value (−0.44 ± 0.05‰) of the average upper continental crust (UCC) (*13*, *29*).

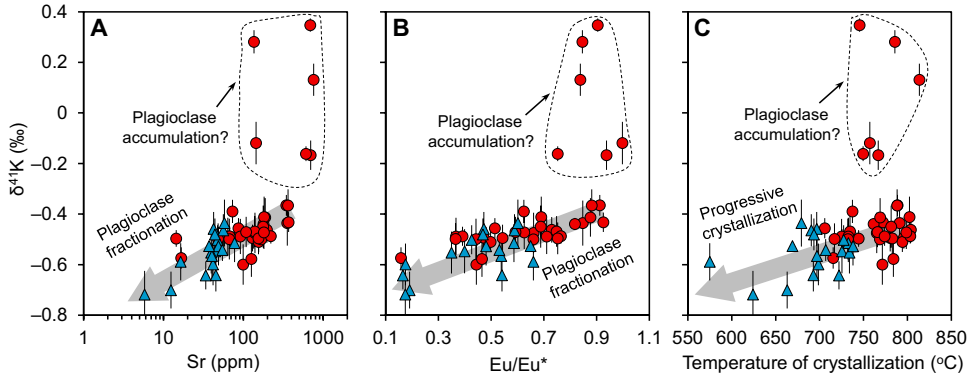

Fig. 2. Covariations of $\delta^{41}K$ value with indicators of plagioclase fractionation and temperature of crystallization. (**A**) $\delta^{41}K$ versus Sr. (**B**) $\delta^{41}K$ versus Eu/Eu*. $Eu/Eu^* = Eu_N/\sqrt{Sm_N \times Gd_N}$, where N denotes normalization by chondrite values (*77*). Eu^{2+} primarily substitutes Ca^{2+} in plagioclase, and thus, separation of plagioclase will lower the Eu/Eu* of residual melts. (**C**) $\delta^{41}K$ versus temperature of crystallization, which is calculated using the monazite saturation thermometry (*78*). The symbols are the same as in Fig. 1.

RESULTS

Fifty-four well-characterized Cenozoic leucogranites from 11 plutons within the Himalayan orogen, covering a broad range of geographic locations and emplacement ages (table S1 and fig. S1), were measured in this study. These leucogranites are primarily composed of light-colored minerals (>90%), e.g., quartz, feldspar, and muscovite, and are subdivided into a biotite-muscovite (termed "two-mica" hereafter) and a muscovite facies based on the mafic mineral assemblage. Two-mica leucogranites typically consist of quartz, plagioclase, K-feldspar, biotite, and muscovite, while tourmaline and garnet are the major mafic minerals in muscovite leucogranites. The $\delta^{41}K$ value varies from −0.72 ± 0.09 to 0.35 ± 0.03‰ in all 54 samples (Fig. 1), which is significantly beyond the range of granitoids reported so far [−0.57 to −0.38‰; (*23*, *29*); see Materials and Methods for the definition of $\delta^{41}K$; its uncertainty is given as 2 SD]. Except for three samples with $\delta^{41}K$ values lower than the average upper continental crust [−0.44 ± 0.05‰; (*29*)], two-mica leucogranites have $\delta^{41}K$ values varying from average crust-like to significantly higher values (−0.51 ± 0.04 to 0.35 ± 0.03‰; $n = 33$), with $\delta^{41}K$ values > −0.2‰ exclusively present in samples containing ≤3 wt % K_2O (Fig. 1B). By contrast, $\delta^{41}K$ values of muscovite leucogranites are overall lower than those of two-mica leucogranites and range from average crust-like to notably lower values (−0.72 ± 0.09 to −0.44 ± 0.09‰; $n = 18$).

DISCUSSION

The large K isotopic variation in the Himalayan leucogranites does not correlate with emplacement age or geographic locations of different plutons (fig. S3A). Instead, $\delta^{41}K$ value covaries with whole-rock chemistry, in particular, trace elements such as Rb, Sr, Ba, and Eu/Eu* (Fig. 2 and fig. S3, B to D). Possible processes that can modify K isotopic compositions of Himalayan leucogranites include chemical weathering, source heterogeneity [e.g., (*32*–*34*)], incongruent partial melting of mica and feldspar during crustal anatexis [e.g., (*35*–*37*)], and crystal-melt separation [e.g., (*38*, *39*)]. Although postemplacement weathering processes could potentially lower the $\delta^{41}K$ values of granites (*40*), 50 of 54 samples are fresh and have chemical index of alteration values [CIA = 50 to 56; see table S1 for definition (*41*)] within the typical range of unweathered granites. Four samples with slightly elevated CIA values (57 to 61) have very high $\delta^{41}K$ values (fig. S4), opposite to the low $\delta^{41}K$ value expected for chemical weathering. Thus, chemical weathering cannot be the main cause for the large

K isotopic variation in our samples. The wide range of $\delta^{41}K$ values in the Himalayan leucogranites must result from either source heterogeneity or magmatic processes, which will be discussed in detail below.

Origins of K isotopic variation in the Himalayan leucogranites

Mica-rich metapelites and feldspar-rich metagreywackes have been regarded as the dominant source lithologies of the Himalayan leucogranites mainly based on the radiogenic (e.g., Sr, Nd, and Hf) and stable (e.g., O and Si) isotopic resemblance to the Himalayan metasediments (*31*, *32*, *34*, *42*) and comparable peraluminous compositions to experimental melts of these metasediments (*36*). Anatexis of these two types of sediments may show distinct chemical and isotopic compositions (*32*–*34*, *42*). Nevertheless, most sediments have $\delta^{41}K$ values similar to the average upper continental crust with none comparable to the highest $\delta^{41}K$ values observed in the two-mica leucogranites (Fig. 1C). Furthermore, clay/mica-rich sediments and feldspar-rich sediments display no obvious difference in the mean $\delta^{41}K$ value. Last, K isotopes in leucogranites do not correlate with radiogenic isotopes (e.g., Sr and Nd) indicative of provenance and lithology of the Himalayan metasedimentary sources (fig. S5) (*32*, *34*). Therefore, the distinct K isotopic signatures between two-mica and muscovite leucogranites cannot be simply explained by source heterogeneity.

Production of leucogranite by anatexis of metasediments is mainly governed by the following reaction: muscovite + plagioclase + quartz ± xH_2O → melt ± K-feldspar ± biotite ± aluminum-silicate, where the proportions of muscovite and plagioclase contributing to the melt strongly depend on the activity of H_2O (*36*). Given the large K isotopic difference between plagioclase and mica (*23*–*26*), incongruent melting of muscovite or plagioclase may fractionate K isotopes between melt and its source. Here, we quantitatively evaluated the extent of K isotope fractionation during anatexis using the same nonmodal partial melting model as previously used to quantify Sr and Nd isotopes (see Materials and Methods for details) (*43*). The results yield <0.07‰ deviation in $\delta^{41}K$ value between melts and the source rock even if a 4‰ K isotope fractionation between plagioclase and mica is assumed (fig. S6). This is consistent with the fact that muscovite has K abundance tens of times higher than plagioclase in metasediments (*36*, *44*); thus, mica is the dominant contributor of K to the melt during anatexis. Therefore, partial melting processes cannot generate the ~1‰ $\delta^{41}K$ variation in the Himalayan leucogranites either.

The most likely process responsible for the progressive decrease in $\delta^{41}K$ value from two-mica leucogranite to muscovite leucogranite is the continuous separation of plagioclase during magmatic differentiation, which is the only known phase that could be significantly enriched in heavy K isotopes (*23*–*26*). This is supported by the positive correlations of $\delta^{41}K$ value with sensitive proxies for plagioclase crystallization, e.g., Sr and Eu/Eu*, and crystallization temperature in most of our leucogranite samples (Fig. 2). These positive trends anchor the $\delta^{41}K$ values of the primary leucogranite melts to average crust-like values. A few two-mica leucogranites with the highest Sr and Eu/Eu* do not follow the trends and have much higher $\delta^{41}K$ (>−0.2‰) values than the average upper crust and any potential source rocks (Fig. 1). They most likely represent the plagioclase-rich cumulates, as supported by the enrichment in plagioclase over K-feldspar (fig. S7).

Both fractional and equilibrium crystallization models were applied to assess the influence of crystal-melt separation on the $\delta^{41}K$ values of the Himalayan leucogranites (see Table 1 for model parameters and Materials and Methods for model details). Given that Rb and Sr behave differently during fractionation of mica and feldspar, the Rb/Sr ratio was modeled to further constrain the degree of crystallization. Note that Rb/Sr in the primary melts can vary greatly because of potentially different source lithologies or different melting reactions (*32*, *35*, *45*). Therefore, 3 two-mica leucogranites having average crust-like K isotopic compositions ($\delta^{41}K$ = −0.39, −0.41, and −0.44‰) and different Rb/Sr ratios (5.65, 1.13, and 0.48) covering the main Rb/Sr range of Himalayan leucogranites were selected as the primary melts in our models. The modal abundance of the crystallizing mineral assemblage throughout the crystallization was determined using the Rhyolite-MELTS software (Fig. 3). Our modeling results match the K isotopic variation in the Himalayan leucogranites. Cumulates produced during both fractional and equilibrium crystallization have similar $\delta^{41}K$ values, both of which are higher than those of the primary melts and proportional to the modal abundance of plagioclase (Fig. 4 and fig. S7). By contrast, fractional crystallization fits data for the isotopically light leucogranites better compared to equilibrium crystallization (Fig. 4). The isotopically lightest leucogranite samples require ~60 to 90% fractional crystallization, which is close to the optimal (~50 to 70%) crystallinity window for efficient separation of high-silica liquids from crystal mushes (*46*).

The above crystallization model is simplified as a closed-system crystal-melt separation. Fractional crystallization of high-silica magmas is often accompanied by wallrock assimilation, late-stage fluid exsolution, and magmatic-hydrothermal interaction (*47*–*51*). Although these processes could also contribute to the K isotopic variation in the Himalayan leucogranites, their contributions are considered minimum. Country rocks of these Himalayan leucogranites are mainly composed of metasediments, and $\delta^{41}K$ values reported for sediments

Table 1. Parameters used in modeling K isotope fractionation during crystal fractionation and accumulation in the Himalayan leucogranites.

Mineral	Mineral/melt partitioning coefficient ($D_i^{mineral/melt}$)			$\Delta^{41}K_{mineral-melt}$ (‰)
	K	Rb	Sr	
Plagioclase*	0.21†	0.05†	6.50‡	2.5§
K-feldspar*	3.12†	0.89†	6.00‡	0§
Biotite	2.28‖	2.00‖	0.04‖	0§
Muscovite	2.53‖	1.60‖	0.05‖	0§
Quartz	0	0	0	–

*The crystallizing plagioclase and K-feldspar used in our model contain 2 and 86 mol % of orthoclase, respectively, according to the compositions of feldspars in the Himalayan two-mica leucogranites (*69*). †Estimated using the empirical relationships based on experimental partitioning of K and Rb between alkali feldspar and peraluminous melt (*19*): $D_K^{feldspar/melt} = 0.142 + 0.035 \times Or$ and $D_{Rb}^{feldspar/melt} = 0.03 + 0.01 \times Or$, where Or is the mole percentage of orthoclase in feldspar. ‡Michael (*66*). §The K isotope fractionation factors between minerals and melt ($\Delta^{41}K_{mineral-melt}$) are assumed to be the same as those between minerals and K-feldspar (*24*), and the rationale for this assumption is discussed in Materials and Methods (see the "Equilibrium crystallization model" section). ‖Icenhower and London (*67*).

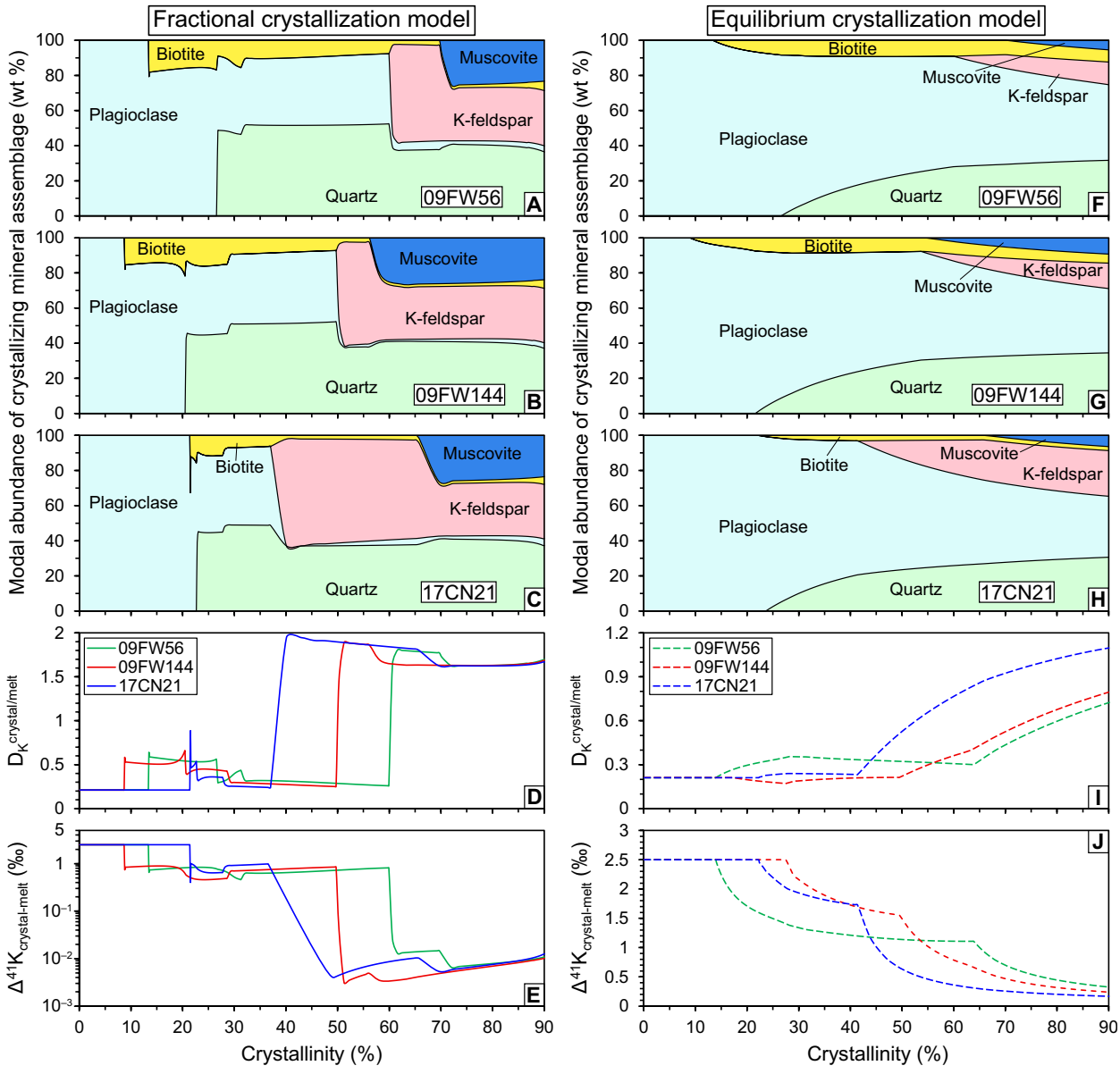

Fig. 3. Numerical modeling of progressive crystallization of the Himalayan leucogranites. The modal percentages of crystallizing mineral assemblages during fractional (**A** to **C**) and equilibrium (**F** to **H**) crystallization of three hypothetical parental leucogranites (09FW56, 09FW144, and 17CN21) were calculated using the Rhyolite-MELTS software. The partitioning coefficient of K ($D_K^{crystal/melt}$) and K isotope fractionation factor ($\Delta^{41}K_{crystal-melt}$) between bulk crystallizing mineral assemblage and melt for the chosen parental leucogranites used in the fractional (**D** and **E**) and equilibrium (**I** and **J**) crystallization models are also plotted. See main text for model details.

vary from crust-like to lighter K isotopic compositions (Fig. 1C). Assimilation by these sediments cannot explain the elevated $\delta^{41}K$ values of those two-mica leucogranites. On the other hand, the Himalayan metasediments have low Rb/Sr (fig. S8); assimilation should have lowered the Rb/Sr of the leucogranites, which is opposite to the higher Rb/Sr for the isotopically lighter muscovite leucogranites (Fig. 4). In addition, these metasediments have K_2O similar to or lower than the muscovite leucogranites (fig. S8), implying that an unrealistically high amount of assimilants would be required to alter leucogranite $\delta^{41}K$ values. Fluid exsolution and fluid-melt interactions can occur at the advanced stage of magmatic differentiation (*48*, *50*, *51*). Partitioning of K between exsolved fluid and granitic melt ($D_K^{fluid/melt}$) is very low in aqueous fluids but linearly increases with the chlorinity of the fluid (m_{Cl}) [$D_K^{fluid/melt} = 0.2 \times m_{Cl}$; (*52*)]. Nevertheless, laboratory experiments and theoretical calculations suggest limited equilibrium K isotope fractionation between Cl-rich fluid and K-rich silicates at the crystallization temperatures of Himalayan leucogranites (fig. S9) (*25*, *53*, *54*). Therefore, both country rock assimilation and late-stage fluid activity have minor effects on K isotopes. Crystal-melt separation, therefore, exerts the first-order control on the large K isotopic variation in the Himalayan leucogranites.

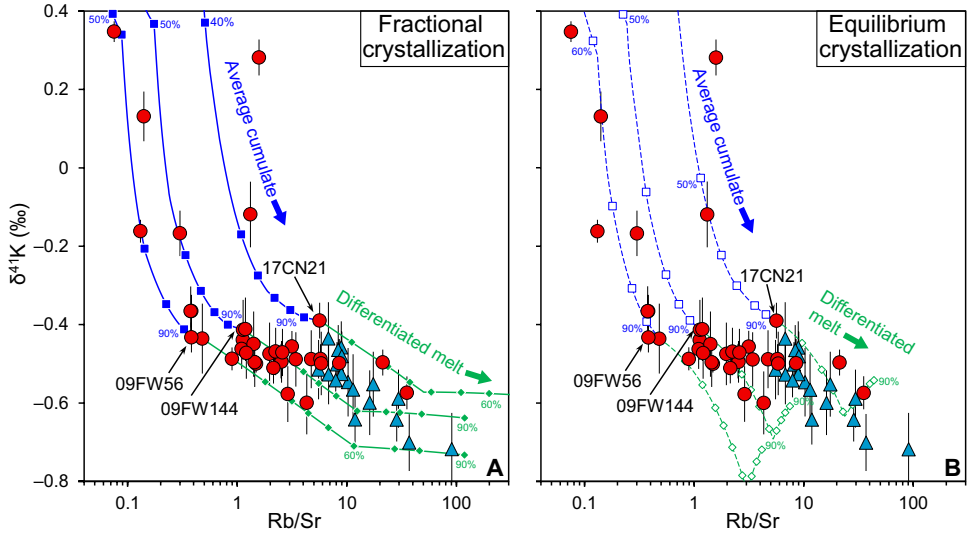

Fig. 4. Modeling evolution of δ^{41}K value and Rb/Sr during crystal fractionation and accumulation in the Himalayan leucogranites. The trajectories represent evolution of the average cumulate (blue) and residual melt (green) during (**A**) fractional and (**B**) equilibrium crystallization of the leucogranites in Fig. 3. Diamonds and squares represent increments of 10% crystallinity. See main text for model details. The symbols are the same as in Fig. 1.

Potassium isotopic tracer of crystal fractionation and accumulation in high-silica magmas

Understanding the processes of felsic magma differentiation is crucial for studying the origin of granitoids (*55*), the relationship between volcanic and plutonic felsic magmas (*56*–*58*), rare-metal (e.g., Sn, W, Nb, Ta, and Be) mineralization associated with high-silica magmatism (*30*, *59*), and catastrophic rhyolitic eruptions (*5*). The recognition of crystal fractionation and accumulation in felsic magmas serves as a prerequisite for addressing the above issues. However, evaluating the degree of fractional crystallization of high-silica magmas and finding felsic cumulates are very challenging. For example, trace element signatures such as subchondritic Nb/Ta and Zr/Hf and tetrad REE (rare earth element) patterns have been regarded as important markers of highly evolved felsic magmas (*30*, *49*), but they are not informative in quantitatively estimating the extent of fractional crystallization. Compatible elements, e.g., Sr, Ba, Eu, and Zr, can be used to identify felsic cumulates because they are enriched in cumulates (*15*, *56*, *60*). However, their enrichment is not often obvious, and the inefficient extraction of interstitial melts from the crystal mush further complicates the diagnostic trace element signatures between cumulates and primary melts (*4*, *15*, *56*). Our study reveals significant K isotope fractionation during both crystal fractionation and cumulation processes in the Himalayan leucogranites. As plagioclase commonly occurs as a major phase during prolonged differentiation of felsic magmas, K isotopes can provide unprecedented insights into the evolution of felsic magmas. Other nontraditional stable isotope systems such as Ca also display detectable fractionation between plagioclase and other Ca-bearing silicates (e.g., hornblende) in felsic rocks and might be used in a similar way to K isotopes to constrain crystal-melt separation in high-silica magmas (*61*, *62*).

MATERIALS AND METHODS

Geological background and sample information

The mid-Eocene to late Miocene leucogranite magmatism is widespread throughout the 2500-km-long Himalayan orogen (fig. S1), which is known as the product of the Cenozoic collision between India and Asia (*37*). The Himalayan orogen can be divided into four units bounded by north-dipping faults from south to north: (i) Sub-Himalayan sequence, mainly comprising Neogene foreland basin sediments; (ii) Lesser Himalayan sequence, which is composed of low-grade Proterozoic metamorphic rocks; (iii) Higher Himalayan sequence (HHS), which is mainly composed of amphibolite- to granulite-facies metasedimentary rocks of Neoproterozoic to Cambrian age, 510 to 480 million years (Ma) of granitic orthogneisses at the middle to lower structural level, and low-grade metamorphic rocks (labeled as Rouqiecun Group) at the upper structural level; (iv) Tethyan Himalayan sequence (THS), which is a suite of low-grade to unmetamorphosed Neoproterozoic to Eocene sediments (fig. S1) (*63*). The Himalayan leucogranites were emplaced within both the HHS and THS, constituting two parallel leucogranite belts. The HHS leucogranites have ages of 25 to 10 Ma and occur primarily as sills and laccoliths along the South Tibetan Detachment System, which separates the HHS from the THS (*30*). By contrast, the THS leucogranites were emplaced over a prolonged period from 46 to 7 Ma and are typically exposed in the cores of the Tethyan or North Himalayan gneiss domes (*30*). Both the HHS and THS leucogranites display broadly similar petrological and geochemical characteristics. Fifty-four samples, including 36 two-mica leucogranites and 18 muscovite leucogranites, were selected for K isotope analysis. The rock type, occurrence, and age of these samples have been summarized in table S1. They were collected from 11 plutons—including Cona, Dingga, and Gaowu from the HHS belt and Ramba, Xiaru, Kuday, Dala, Suozuo, Sakya, Lhagoi Kangri, Malashan, and Paikucuo from the THS belt—and have ages (44 to 8 Ma) covering the main stages of the Himalayan leucogranite magmatism (fig. S1).

Potassium isotopic analysis

Potassium isotopic compositions were determined at the Isotope Laboratory of the University of Washington, Seattle, following a previously established protocol (*64*, *65*). A brief description of this method, together with some minor improvements, was summarized

here. Around 5 to 15 mg of whole-rock powders were successively digested in Teflon beakers with HF-HNO_3 mixture, HCl-HNO_3 mixture, concentrated HNO_3, and 0.5 N HNO_3.To achieve purification of K, an aliquot of solution containing 100 to 200 μg of K was passed through a column filled with 2 ml of Bio-Rad AG50W-X8 (200- to 400-mesh) resin and was eluted using 0.5 N HNO_3. This procedure was performed twice to ensure effective purification with a K yield of >99%. The whole procedural blank contains <10 ng of K, which is negligible compared to the amount of K loaded onto the columns.

The isotopic ratios were measured on a Nu Plasma II multi-collector inductively coupled plasma mass spectrometer using the standard-sample bracketing method to correct the instrumental mass bias. The K concentrations of both sample and bracketing standard National Institute of Standards and Technology (NIST) standard reference material (SRM) 3141a were diluted to 3 parts per million (ppm) in 3% HNO_3 before measurement. To overcome the strong isobaric interference of $^{40}Ar^1H^+$ on ^{41}K, solutions were introduced into the plasma using a CETAC Aridus II desolvating nebulizer system at the radio frequency power of 700 to 750 W. The ^{39}K and ^{41}K signals were measured simultaneously at an interference-free shoulder in pseudo-high-resolution mode. An ice bucket with a constant temperature of ~5°C was used to store the waste acid bottle of the Aridus II, which helps to improve the signal stability and sensitivity. The intensity of ^{39}K signal is typically 6 to 8 V for a 3-ppm solution. The final data are reported in $\delta^{41}K$ notation against NIST SRM 3141a as

$$\delta^{41}\mathrm{K}\,(‰) = \left[\frac{(^{41}\mathrm{K}/^{39}\mathrm{K})_{\mathrm{sample}}}{(^{41}\mathrm{K}/^{39}\mathrm{K})_{\mathrm{NIST\ SRM\ 3141a}}} - 1\right] \times 1000$$

Accuracy and reproducibility were assessed on the basis of the analysis of three granite standards (G-2, GS-N, and JG-1) and one rhyolite standard (RGM-1), which were dissolved and processed through column chemistry together with the samples. Their $\delta^{41}K$ values agree with the published values (table S2). Multiple analyses on these rock standards also yielded consistent results.

Modeling K isotope fractionation during anatexis of metapelites

The melting reaction is described as: muscovite + plagioclase + quartz ± xH_2O → melt ± K-feldspar ± biotite ± aluminum-silicate. The K isotopic composition of the source rock ($\delta^{41}K_{source}$) is given by

$$\delta^{41}\mathrm{K}_{\mathrm{source}} = \frac{\sum_{\alpha=1}^{n}(\mathrm{X}^{0}_{\mathrm{mineral}\,\alpha} \times [\mathrm{K_2O}]_{\mathrm{mineral}\,\alpha} \times \delta^{41}\mathrm{K}_{\mathrm{mineral}\,\alpha})}{\sum_{\alpha=1}^{n}(\mathrm{X}^{0}_{\mathrm{mineral}\,\alpha} \times [\mathrm{K_2O}]_{\mathrm{mineral}\,\alpha})} \quad (1)$$

where $X^0_{mineral\ \alpha}$, $[K_2O]_{mineral\ \alpha}$, and $\delta^{41}K_{mineral\ \alpha}$ are the mass proportion of mineral α in the source rock, K_2O content of mineral α, and $\delta^{41}K$ value of mineral α, respectively. The model parameters are presented in table S3.

We assume a constant K_2O content and a $\delta^{41}K$ value for each mineral during melting processes. The K isotopic composition of melt ($\delta^{41}K_{melt}$) can be calculated using the following equation

$$\delta^{41}\mathrm{K}_{\mathrm{melt}} = \frac{\sum_{\alpha=1}^{n}(\mathrm{X}^{\mathrm{L}}_{\mathrm{mineral}\,\alpha} \times [\mathrm{K_2O}]_{\mathrm{mineral}\,\alpha} \times \delta^{41}\mathrm{K}_{\mathrm{mineral}\,\alpha})}{\sum_{\alpha=1}^{n}(\mathrm{X}^{\mathrm{L}}_{\mathrm{mineral}\,\alpha} \times [\mathrm{K_2O}]_{\mathrm{mineral}\,\alpha})} \quad (2)$$

where $X^L_{mineral\ \alpha}$ is the mass proportion of mineral α entering the melt. The mass proportions of reacting phases entering the melt at different degrees of melting are from table 2 in the work of Patiño Douce and Harris (*36*). The $\delta^{41}K$ evolution in melts during partial melting of metasediments at 6 and 10 kbar both without H_2O and with 2 to 4 wt % H_2O is reported in fig. S6.

Equilibrium crystallization model

The crystals and melt remain in equilibrium throughout crystallization in this model, so K isotopic compositions of differentiated melt ($\delta^{41}K_{melt}$) and complementary cumulate ($\delta^{41}K_{cumulate}$) can be calculated using the isotope mass balance equations

$$\delta^{41}\mathrm{K}_{\mathrm{initial\ melt}} = f^{\mathrm{K}}_{\mathrm{melt}} \times \delta^{41}\mathrm{K}_{\mathrm{melt}} + (1 - f^{\mathrm{K}}_{\mathrm{melt}}) \times \delta^{41}\mathrm{K}_{\mathrm{cumulate}} \quad (3)$$

$$\delta^{41}\mathrm{K}_{\mathrm{melt}} = \delta^{41}\mathrm{K}_{\mathrm{cumulate}} - \Delta^{41}\mathrm{K}_{\mathrm{crystal-melt}} \quad (4)$$

where f^K_{melt} is the mass fraction of K remaining in melt and $\Delta^{41}K_{crystal\ -\ melt}$ is the K isotope fractionation factor between crystallizing assemblage and melt. f^K_{melt} equals $\frac{(F \times C^K_{melt})}{C^K_{initial\ melt}}$, and the relationship between the degree of crystallization (F) and K concentrations of melt (C^K_{melt}) is governed by the batch crystallization equation

$$\mathrm{C}^{\mathrm{K}}_{\mathrm{melt}} = \frac{\mathrm{C}^{\mathrm{K}}_{\mathrm{initial\ melt}}}{(\mathrm{D}^{\mathrm{crystal/melt}}_{\mathrm{K}} - 1) \times \mathrm{F} + 1} \quad (5)$$

where $D^{crystal/melt}_K$ is the bulk partitioning coefficient of K between crystallizing assemblage and melt.

$D^{crystal/melt}_K$ and $\Delta^{41}K_{crystal-melt}$ can be obtained by

$$\mathrm{D}^{\mathrm{crystal/melt}}_{\mathrm{K}} = \sum_{\alpha=1}^{n}(\mathrm{D}^{\mathrm{mineral}\,\alpha/\mathrm{melt}}_{\mathrm{K}} \times \mathrm{X}_{\mathrm{mineral}\,\alpha}) \quad (6)$$

$$\Delta^{41}\mathrm{K}_{\mathrm{crystal-melt}} = \frac{\sum_{\alpha=1}^{n}(\mathrm{D}^{\mathrm{mineral}\,\alpha/\mathrm{melt}}_{\mathrm{K}} \times X_{\mathrm{mineral}\,\alpha} \times \Delta^{41}\mathrm{K}_{\mathrm{mineral}\,\alpha-\mathrm{melt}})}{\sum_{\alpha=1}^{n}(\mathrm{D}^{\mathrm{mineral}\,\alpha/\mathrm{melt}}_{\mathrm{K}} \times \mathrm{X}_{\mathrm{mineral}\,\alpha})} \quad (7)$$

where $D^{mineral/melt}_K$, $\Delta^{41}K_{mineral\ -\ melt}$, and $X_{mineral}$ are the mineral/melt partitioning coefficient for K, mineral-melt K isotope fractionation factor, and weight portion of mineral in crystallizing assemblage, respectively.

Partitioning of K between major K-bearing minerals and peraluminous melt has been well documented (*66*, *67*), but $\Delta^{41}K_{mineral-melt}$ is still unknown. Considering that the K—O bond length in silicate glass (3.00 to 3.06 Å) is close to that in orthoclase (2.94 Å) (*68*), we used the $\Delta^{41}K_{mineral-orthoclase}$ as an approximation to the $\Delta^{41}K_{mineral-melt}$ in our model. The $\delta^{41}K$ value of feldspar is inversely correlated with its orthoclase content (*23*, *24*, *26*); orthoclase-poor plagioclase [Or = 3 mole percent (mol %)] can be isotopically heavier than the coexisting K-rich feldspar in equilibrium (Or > 50 mol %) by 2.5‰ (*24*). By contrast, K isotope fractionation between mica minerals and K-rich feldspar (Or > 50%) is near zero at magmatic temperatures (*23*–*25*, *54*). The feldspar in Himalayan leucogranites is composed of two nearly pure endmembers: albite-dominant plagioclase (Ab >78 mol % and Or < 3 mol %) and orthoclase-dominant K-feldspar (Or > 83 mol %) (*69*). Therefore, constant $\Delta^{41}K_{plagiocalse-melt}$ of 2.5‰, $\Delta^{41}K_{K-feldspar-melt}$ of 0‰, $\Delta^{41}K_{bitotite-melt}$ of 0‰, and $\Delta^{41}K_{muscovite-melt}$ of 0‰ were adopted.

The modal abundance of the crystallizing mineral assemblage varies with temperature as crystallization proceeds. In the case of equilibrium crystallization, $X_{mineral}$ is the same as the modal abundance of minerals in the average cumulate. Here, we applied the thermodynamic modeling software Rhyolite-MELTS to determine the modal mineralogy of the average cumulate throughout the crystallization (*70*). The calculations were performed from super-solidus (F = 0%, 900°C) to near-solidus (F = 90%, 640°C) in 0.5°C steps under the same condition as crystallization experiments on Himalayan leucogranites [pressure = 400 MPa, oxygen fugacity = -0.5 log units of the fayalite-magnetite-quartz oxygen buffer (FMQ-0.5), initial water content = 6 wt %; (*71*)]. Note that Rhyolite-MELTS modeling works best for metaluminous melts (*70*). If the phases in the Rhyolite-MELTS program were not suppressed, then our modeling produced orthopyroxene and leucite, which are never found in the Himalayan leucogranites. To better reproduce the crystallizing assemblage, only the five most common minerals (i.e., quartz, plagioclase, K-feldspar, biotite, and muscovite) in the Himalayan leucogranites were chosen as potential solid phases in our models. Other subordinate minerals such as tourmaline and garnet barely contain K, Rb, and Sr, and thus, their absence has little effect on our modeling $\delta^{41}K$ and Rb/Sr variations. This modeling approach predicts the earlier crystallization of plagioclase and biotite relative to K-feldspar and muscovite (Fig. 3, A to C), which is consistent with the sequence constrained by both microscopic observations and crystallization experiments on two-mica leucogranites (*38*, *71*).

The Rb and Sr concentrations of the differentiated melt can be calculated using Eq. 5. Those of the cumulate are estimated by a mass balance equation (taking Rb as an example)

$$C^{Rb}_{initial\ melt} = F \times C^{Rb}_{melt} + (1 - F) \times C^{Rb}_{cumulate} \quad (8)$$

Fractional crystallization model

During fractional crystallization, crystals are not in equilibrium with the differentiated melt anymore once they are segregated. The modal mineralogy of the crystallizing assemblage over the differentiation sequence is estimated via the Rhyolite-MELTS modeling under the same conditions described in the equilibrium crystallization model but in the "fractionate solids" mode (*70*).

$D_K^{crystal/melt}$ and $\Delta^{41}K_{crystal-melt}$ are recalculated at every step of 0.5°C using Eqs. 6 and 7, and we assume a constant modal abundance of crystallizing mineral assemblage for each step. The K concentration and isotopic composition of the differentiated melt at step *i* are estimated using the Rayleigh distillation equations

$$C^{K,i}_{melt} = C^{K,i-1}_{melt} \times (1 - F^i)^{(D_K^{crystal/melt} - 1)} \quad (9)$$

$$\delta^{41}K^i_{melt} = \delta^{41}K^{i-1}_{melt} + \Delta^{41}K_{crystal-melt} \times \ln(f^{K,i}_{melt}) \quad (10)$$

F^i is the degree of crystallization for the 0.5°C interval at step *i* and equals $\frac{(M^i_{melt} - M^{i-1}_{melt})}{M^{i-1}_{melt}}$, where M_{melt} is the mass of remaining melt. $f^{K,i}_{melt}$ is the mass fraction of K in melt *i* relative to melt *i* − 1 and equals $\frac{(F^i \times C^{K,i}_{melt})}{C^{K,i-1}_{melt}}$.

The K isotopic composition of average cumulate is determined using the isotope mass balance Eq. 3. The Rb and Sr concentrations of the differentiated melt and average cumulate can be obtained by Eqs. 8 and 9.

SUPPLEMENTARY MATERIALS

Supplementary material for this article is available at https://science.org/doi/10.1126/sciadv.abo4492

REFERENCES AND NOTES

1. C. B. Keller, B. Schoene, M. Barboni, K. M. Samperton, J. M. Husson, Volcanic–plutonic parity and the differentiation of the continental crust. *Nature* **523**, 301–307 (2015).
2. C.-T. A. Lee, O. Bachmann, How important is the role of crystal fractionation in making intermediate magmas? Insights from Zr and P systematics. *Earth Planet. Sci. Lett.* **393**, 266–274 (2014).
3. R. S. J. Sparks, H. E. Huppert, Density changes during the fractional crystallization of basaltic magmas: Fluid dynamic implications. *Contrib. Mineral. Petrol.* **85**, 300–309 (1984).
4. C.-T. A. Lee, D. M. Morton, High silica granites: Terminal porosity and crystal settling in shallow magma chambers. *Earth Planet. Sci. Lett.* **409**, 23–31 (2015).
5. O. Bachmann, G. W. Bergantz, On the origin of crystal-poor rhyolites: Extracted from batholithic crystal mushes. *J. Petrol.* **45**, 1565–1582 (2004).
6. F. Bea, Crystallization dynamics of granite magma chambers in the absence of regional stress: Multiphysics modeling with natural examples. *J. Petrol.* **51**, 1541–1569 (2010).
7. B. D. Marsh, Dynamics of magmatic systems. *Elements* **2**, 287–292 (2006).
8. D. Martin, R. Nokes, A fluid-dynamical study of crystal settling in convecting magmas. *J. Petrol.* **30**, 1471–1500 (1989).
9. A. J. Schaen, B. Schoene, J. Dufek, B. S. Singer, M. P. Eddy, B. R. Jicha, J. M. Cottle, Transient rhyolite melt extraction to produce a shallow granitic pluton. *Sci. Adv.* **7**, eabf0604 (2021).
10. A. F. Glazner, Magmatic life at low Reynolds number. *Geology* **42**, 935–938 (2014).
11. D. McKenzie, The extraction of magma from the crust and mantle. *Earth Planet. Sci. Lett.* **74**, 81–91 (1985).
12. W. Hildreth, Volcanological perspectives on Long Valley, Mammoth Mountain, and Mono Craters: Several contiguous but discrete systems. *J. Volcanol. Geotherm. Res.* **136**, 169–198 (2004).
13. R. Rudnick, S. Gao, in *Treatise on Geochemistry* (Elsevier, ed. 2, 2014), vol. 3, pp. 1–51.
14. M. B. Holness, Cumulates and layered igneous rocks, in *Encyclopedia of Geology*, D. Alderton, S. A. Elias, Eds. (Academic Press, ed. 2, 2021), pp. 99–112.
15. C. D. Deering, O. Bachmann, Trace element indicators of crystal accumulation in silicic igneous rocks. *Earth Planet. Sci. Lett.* **297**, 324–331 (2010).
16. A. F. Glazner, J. M. Bartley, D. S. Coleman, W. Gray, R. Z. Taylor, Are plutons assembled over millions of years by amalgamation from small magma chambers? *GSA Today* **14**, 4–12 (2004).
17. C. Annen, From plutons to magma chambers: Thermal constraints on the accumulation of eruptible silicic magma in the upper crust. *Earth Planet. Sci. Lett.* **284**, 409–416 (2009).
18. B. Chappell, Aluminium saturation in I-and S-type granites and the characterization of fractionated haplogranites. *Lithos* **46**, 535–551 (1999).
19. J. Icenhower, D. London, Experimental partitioning of Rb, Cs, Sr, and Ba between alkali feldspar and peraluminous melt. *Am. Mineral.* **81**, 719–734 (1996).
20. F.-Y. Wu, B.-M. Jahn, S. A. Wilde, C.-H. Lo, T.-F. Yui, Q. Lin, W.-C. Ge, D.-Y. Sun, Highly fractionated I-type granites in NE China (I): Geochronology and petrogenesis. *Lithos* **66**, 241–273 (2003).
21. A. F. Glazner, B. R. Johnson, Late crystallization of K-feldspar and the paradox of megacrystic granites. *Contrib. Mineral. Petrol.* **166**, 777–799 (2013).
22. L. E. Morgan, D. P. S. Ramos, B. Davidheiser-Kroll, J. Faithfull, N. S. Lloyd, R. M. Ellam, J. A. Higgins, High-precision $^{41}K/^{39}K$ measurements by MC-ICP-MS indicate terrestrial variability of $\delta^{41}K$. *J. Anal. At. Spectrom* **33**, 175–186 (2018).
23. W. W. Kuhnel, S. B. Jacobsen, Y. Li, Y. Ku, M. I. Petaev, S. Huang, Z. Wu, K. Wang, High-temperature inter-mineral potassium isotope fractionation: Implications for K–Ca–Ar chronology. *ACS Earth and Space Chem.* **5**, 2740–2754 (2021).
24. T.-Y. Huang, F.-Z. Teng, Z.-Z. Wang, Y. He, F.-Y. Wu, paper presented at the Goldschmidt Conference, Honolulu, Hawai'i, USA, 13 July 2022.
25. H. Zeng, V. F. Rozsa, N. X. Nie, Z. Zhang, T. A. Pham, G. Galli, N. Dauphas, Ab initio calculation of equilibrium isotopic fractionations of potassium and rubidium in minerals and water. *ACS Earth and Space Chem.* **3**, 2601–2612 (2019).
26. Y. Li, W. Wang, S. Huang, K. Wang, Z. Wu, First-principles investigation of the concentration effect on equilibrium fractionation of K isotopes in feldspars. *Geochim. Cosmochim. Acta* **245**, 374–384 (2019).
27. B. Tuller-Ross, P. S. Savage, H. Chen, K. Wang, Potassium isotope fractionation during magmatic differentiation of basalt to rhyolite. *Chem. Geol.* **525**, 37–45 (2019).
28. Y. Hu, F. Z. Teng, R. T. Helz, C. Chauvel, Potassium isotope fractionation during magmatic differentiation and the composition of the mantle. *J. Geophys. Res. Solid Earth* **126**, e2020JB021543 (2021).
29. T.-Y. Huang, F.-Z. Teng, R. L. Rudnick, X.-Y. Chen, Y. Hu, Y.-S. Liu, F.-Y. Wu, Heterogeneous potassium isotopic composition of the upper continental crust. *Geochim. Cosmochim. Acta* **278**, 122–136 (2020).
30. F.-Y. Wu, X.-C. Liu, Z.-C. Liu, R.-C. Wang, L. Xie, J.-M. Wang, W.-Q. Ji, L. Yang, C. Liu, G. P. Khanal, S.-X. He, Highly fractionated Himalayan leucogranites and associated rare-metal mineralization. *Lithos* **352**, 105319 (2020).

31. T. N. Hopkinson, N. B. W. Harris, C. J. Warren, C. J. Spencer, N. M. W. Roberts, M. S. A. Horstwood, R. R. Parrish, The identification and significance of pure sediment-derived granites. *Earth Planet. Sci. Lett.* **467**, 57–63 (2017).
32. S. Guillot, P. Le Fort, Geochemical constraints on the bimodal origin of High Himalayan leucogranites. *Lithos* **35**, 221–234 (1995).
33. P. J. Sylvester, Post-collisional strongly peraluminous granites. *Lithos* **45**, 29–44 (1998).
34. M. Ji, X.-Y. Gao, Y.-F. Zheng, Geochemical evidence for partial melting of progressively varied crustal sources for leucogranites during the Oligocene–Miocene in the Himalayan orogen. *Chem. Geol.* **589**, 120674 (2022).
35. L.-E. Gao, L. Zeng, P. D. Asimow, Contrasting geochemical signatures of fluid-absent versus fluid-fluxed melting of muscovite in metasedimentary sources: The Himalayan leucogranites. *Geology* **45**, 39–42 (2017).
36. A. E. Patiño Douce, N. Harris, Experimental constraints on Himalayan anatexis. *J. Petrol.* **39**, 689–710 (1998).
37. N. Harris, M. Ayres, J. Massey, Geochemistry of granitic melts produced during the incongruent melting of muscovite: Implications for the extraction of Himalayan leucogranite magmas. *J. Geophys. Res. Solid Earth* **100**, 15767–15777 (1995).
38. B. Scaillet, C. France-Lanord, P. Le Fort, Badrinath-Gangotri plutons (Garhwal, India): Petrological and geochemical evidence for fractionation processes in a high Himalayan leucogranite. *J. Volcanol. Geotherm. Res.* **44**, 163–188 (1990).
39. Z.-C. Liu, F.-Y. Wu, L. Ding, X.-C. Liu, J.-G. Wang, W.-Q. Ji, Highly fractionated Late Eocene (~ 35 Ma) leucogranite in the Xiaru Dome, Tethyan Himalaya, South Tibet. *Lithos* **240**, 337–354 (2016).
40. F.-Z. Teng, Y. Hu, J.-L. Ma, G.-J. Wei, R. L. Rudnick, Potassium isotope fractionation during continental weathering and implications for global K isotopic balance. *Geochim. Cosmochim. Acta* **278**, 261–271 (2020).
41. H. Nesbitt, G. M. Young, Early Proterozoic climates and plate motions inferred from major element chemistry of lutites. *Nature* **299**, 715–717 (1982).
42. X.-C. Liu, X.-H. Li, Y. Liu, L. Yang, Q.-L. Li, F.-Y. Wu, H.-M. Yu, F. Huang, Insights into the origin of purely sediment-derived Himalayan leucogranites: Si–O isotopic constraints. *Sci. Bull.* **63**, 1243–1245 (2018).
43. L. Zeng, P. D. Asimow, J. B. Saleeby, Coupling of anatectic reactions and dissolution of accessory phases and the Sr and Nd isotope systematics of anatectic melts from a metasedimentary source. *Geochim. Cosmochim. Acta* **69**, 3671–3682 (2005).
44. S. Inger, N. B. W. Harris, Tectonothermal evolution of the High Himalayan crystalline sequence, Langtang Valley, northern Nepal. *J. Metam. Geol.* **10**, 439–452 (1992).
45. S. Inger, N. Harris, Geochemical constraints on leucogranite magmatism in the Langtang Valley, Nepal Himalaya. *J. Petrol.* **34**, 345–368 (1993).
46. J. Dufek, O. Bachmann, Quantum magmatism: Magmatic compositional gaps generated by melt-crystal dynamics. *Geology* **38**, 687–690 (2010).
47. D. J. DePaolo, Trace element and isotopic effects of combined wallrock assimilation and fractional crystallization. *Earth Planet. Sci. Lett.* **53**, 189–202 (1981).
48. M. Bau, Controls on the fractionation of isovalent trace elements in magmatic and aqueous systems: Evidence from Y/Ho, Zr/Hf, and lanthanide tetrad effect. *Contrib. Mineral. Petrol.* **123**, 323–333 (1996).
49. W. Irber, The lanthanide tetrad effect and its correlation with K/Rb, Eu/Eu∗, Sr/Eu, Y/Ho, and Zr/Hf of evolving peraluminous granite suites. *Geochim. Cosmochim. Acta* **63**, 489–508 (1999).
50. B.-m. Jahn, F. Wu, R. Capdevila, F. Martineau, Z. Zhao, Y. Wang, Highly evolved juvenile granites with tetrad REE patterns: The Woduhe and Baerzhe granites from the Great Xing'an Mountains in NE China. *Lithos* **59**, 171–198 (2001).
51. A. Heimann, B. L. Beard, C. M. Johnson, The role of volatile exsolution and sub-solidus fluid/rock interactions in producing high $^{56}Fe/^{54}$ Fe ratios in siliceous igneous rocks. *Geochim. Cosmochim. Acta* **72**, 4379–4396 (2008).
52. Z. Zajacz, W. E. Halter, T. Pettke, M. Guillong, Determination of fluid/melt partition coefficients by LA-ICPMS analysis of co-existing fluid and silicate melt inclusions: Controls on element partitioning. *Geochim. Cosmochim. Acta* **72**, 2169–2197 (2008).
53. W. Li, K. D. Kwon, S. Li, B. L. Beard, Potassium isotope fractionation between K-salts and saturated aqueous solutions at room temperature: Laboratory experiments and theoretical calculations. *Geochim. Cosmochim. Acta* **214**, 1–13 (2017).
54. Y. Li, W. Wang, Z. Wu, S. Huang, First-principles investigation of equilibrium K isotope fractionation among K-bearing minerals. *Geochim. Cosmochim. Acta* **264**, 30–42 (2019).
55. J.-F. Moyen, V. Janoušek, O. Laurent, O. Bachmann, J.-B. Jacob, F. Farina, P. Fiannacca, A. Villaros, Crustal melting vs. fractionation of basaltic magmas: Part 1, granites and paradigms. *Lithos* **402**, 106291 (2021).
56. S. E. Gelman, C. D. Deering, O. Bachmann, C. Huber, F. J. Gutiérrez, Identifying the crystal graveyards remaining after large silicic eruptions. *Earth Planet. Sci. Lett.* **403**, 299–306 (2014).
57. O. Bachmann, G. W. Bergantz, Rhyolites and their source mushes across tectonic settings. *J. Petrol.* **49**, 2277–2285 (2008).
58. A. F. Glazner, D. S. Coleman, J. M. Bartley, The tenuous connection between high-silica rhyolites and granodiorite plutons. *Geology* **36**, 183–186 (2008).
59. C. Ballouard, M. Poujol, P. Boulvais, Y. Branquet, R. Tartese, J.-L. Vigneresse, Nb-Ta fractionation in peraluminous granites: A marker of the magmatic-hydrothermal transition. *Geology* **44**, 231–234 (2016).
60. A. J. Schaen, J. M. Cottle, B. S. Singer, C. B. Keller, N. Garibaldi, B. Schoene, Complementary crystal accumulation and rhyolite melt segregation in a late Miocene Andean pluton. *Geology* **45**, 835–838 (2017).
61. M. A. Antonelli, T. Mittal, A. McCarthy, B. Tripoli, J. M. Watkins, D. J. DePaolo, Ca isotopes record rapid crystal growth in volcanic and subvolcanic systems. *Proc. Natl. Acad. Sci.* **116**, 20315–20321 (2019).
62. Y. Wang, Y. He, H. Wu, C. Zhu, S. Huang, J. Huang, Calcium isotope fractionation during crustal melting and magma differentiation: Granitoid and mineral-pair perspectives. *Geochim. Cosmochim. Acta* **259**, 37–52 (2019).
63. A. Yin, Cenozoic tectonic evolution of the Himalayan orogen as constrained by along-strike variation of structural geometry, exhumation history, and foreland sedimentation. *Earth Sci. Rev.* **76**, 1–131 (2006).
64. Y. Hu, X.-Y. Chen, Y.-K. Xu, F.-Z. Teng, High-precision analysis of potassium isotopes by HR-MC-ICPMS. *Chem. Geol.* **493**, 100–108 (2018).
65. Y.-K. Xu, Y. Hu, X.-Y. Chen, T.-Y. Huang, R. S. Sletten, D. Zhu, F.-Z. Teng, Potassium isotopic compositions of international geological reference materials. *Chem. Geol.* **513**, 101–107 (2019).
66. P. J. Michael, Chemical differentiation of the Cordillera Paine granite (southern Chile) by *in situ* fractional crystallization. *Contrib. Mineral. Petrol.* **87**, 179–195 (1984).
67. J. Icenhower, D. London, An experimental study of element partitioning among biotite, muscovite, and coexisting peraluminous silicic melt at 200 MPa (H_2O). *Am. Mineral.* **80**, 1229–1251 (1995).
68. W. E. Jackson, G. E. Brown Jr., C. W. Ponader, X-ray absorption study of the potassium coordination environment in glasses from the $NaAlSi_3O_8$-$KAlSi_3O_8$ binary: Structural implications for the mixed-alkali effect. *J. Non Cryst. Solids* **93**, 311–322 (1987).
69. Z.-C. Liu, F.-Y. Wu, X.-C. Liu, J.-G. Wang, R. Yin, Z.-L. Qiu, W.-Q. Ji, L. Yang, Mineralogical evidence for fractionation processes in the Himalayan leucogranites of the Ramba Dome, southern Tibet. *Lithos* **340**, 71–86 (2019).
70. G. A. R. Gualda, M. S. Ghiorso, R. V. Lemons, T. L. Carley, Rhyolite-MELTS: A modified calibration of MELTS optimized for silica-rich, fluid-bearing magmatic systems. *J. Petrol.* **53**, 875–890 (2012).
71. B. Scaillet, M. Pichavant, J. Roux, Experimental crystallization of leucogranite magmas. *J. Petrol.* **36**, 663–705 (1995).
72. W. Li, S. Li, B. L. Beard, Geological cycling of potassium and the K isotopic response: Insights from loess and shales. *Acta Geochim.* **38**, 508–516 (2019).
73. C. A. Parendo, S. B. Jacobsen, J.-I. Kimura, R. N. Taylor, Across-arc variations in K-isotope ratios in lavas of the Izu arc: Evidence for progressive depletion of the slab in K and similarly mobile elements. *Earth Planet. Sci. Lett.* **578**, 117291 (2022).
74. Z.-Z. Wang, F.-Z. Teng, V. Busigny, S.-A. Liu, Evidence from HP/UHP metasediments for recycling of isotopically heterogeneous potassium into the mantle. *Am. Mineral.* **107**, 350–356 (2022).
75. Y. Hu, F.-Z. Teng, T. Plank, C. Chauvel, Potassium isotopic heterogeneity in subducting oceanic plates. *Sci. Adv.* **6**, eabb2472 (2020).
76. X. Li, G. Han, M. Liu, J. Liu, Q. Zhang, R. Qu, Potassium and its isotope behaviour during chemical weathering in a tropical catchment affected by evaporite dissolution. *Geochim. Cosmochim. Acta* **316**, 105–121 (2022).
77. S. s. Sun, W. F. McDonough, Chemical and isotopic systematics of oceanic basalts: Implications for mantle composition and processes. *Geol. Soc. Spec. Publ.* **42**, 313–345 (1989).
78. J.-M. Montel, A model for monazite/melt equilibrium and application to the generation of granitic magmas. *Chem. Geol.* **110**, 127–146 (1993).
79. P. D. Maniar, P. M. Piccoli, Tectonic discrimination of granitoids. *Geol. Soc. Am. Bull.* **101**, 635–643 (1989).
80. L.-E. Gao, L. Zeng, J. Gao, Z. Shang, K. Hou, Q. Wang, Oligocene crustal anatexis in the Tethyan Himalaya, Southern Tibet. *Lithos* **264**, 201–209 (2016).
81. Z.-C. Liu, F.-Y. Wu, W.-Q. Ji, J.-G. Wang, C.-Z. Liu, Petrogenesis of the Ramba leucogranite in the Tethyan Himalaya and constraints on the channel flow model. *Lithos* **208-209**, 118–136 (2014).
82. H. Zhang, N. Harris, R. Parrish, S. Kelley, L. Zhang, N. Rogers, T. Argles, J. King, Causes and consequences of protracted melting of the mid-crust exposed in the North Himalayan antiform. *Earth Planet. Sci. Lett.* **228**, 195–212 (2004).
83. L. Zeng, L.-E. Gao, K. Xie, J. Liu-Zeng, Mid-Eocene high Sr/Y granites in the Northern Himalayan Gneiss Domes: Melting thickened lower continental crust. *Earth Planet. Sci. Lett.* **303**, 251–266 (2011).
84. L.-E. Gao, L. Zeng, Fluxed melting of metapelite and the formation of Miocene high-CaO two-mica granites in the Malashan gneiss dome, southern Tibet. *Geochim. Cosmochim. Acta* **130**, 136–155 (2014).

85. S.-X. He, X.-C. Liu, L. Yang, J.-M. Wang, F.-Y. Hu, F.-Y. Wu, Multistage magmatism recorded in a single gneiss dome: Insights from the Lhagoi Kangri leucogranites, Himalayan orogen. *Lithos* **398**, 106222 (2021).
86. Q. Shi, Y. He, Z. Zhao, D. Liu, N. Harris, D. C. Zhu, Petrogenesis of Himalayan Leucogranites: Perspective from a combined elemental and Fe-Sr-Nd isotope study. *J. Geophys. Res. Solid Earth* **126**, e2021JB021839 (2021).
87. Z. Guo, M. Wilson, The Himalayan leucogranites: Constraints on the nature of their crustal source region and geodynamic setting. *Gondw. Res.* **22**, 360–376 (2012).
88. P. Gao, Y.-F. Zheng, Z.-F. Zhao, G.-C. Sun, Source diversity in controlling the compositional diversity of Cenozoic granites in the Tethyan Himalaya. *Lithos* **388**, 106072 (2021).
89. A. Richards, T. Argles, N. Harris, R. Parrish, T. Ahmad, F. Darbyshire, E. Draganits, Himalayan architecture constrained by isotopic tracers from clastic sediments. *Earth Planet. Sci. Lett.* **236**, 773–796 (2005).
90. A. B. Aikman, T. M. Harrison, J. Hermann, The origin of Eo- and Neo-himalayan granitoids, Eastern Tibet. *J. Asian Earth Sci.* **58**, 143–157 (2012).
91. M. Ji, X.-Y. Gao, Y.-F. Zheng, Z.-Y. Meng, P. Gao, Metapelites record two episodes of decompressional metamorphism in the Himalayan orogen. *Lithos* **394-395**, 106183 (2021).
92. A. Richards, R. Parrish, N. Harris, T. Argles, L. Zhang, Correlation of lithotectonic units across the eastern Himalaya, Bhutan. *Geology* **34**, 341–344 (2006).
93. H. Zhang, N. Harris, R. Parrish, L. Zhang, Z. Zhao, U-Pb ages of Kude and Sajia leucogranites in Sajia dome from North Himalaya and their geological implications. *Chin. Sci. Bull.* **49**, 2087–2092 (2004).
94. A. B. Aikman, T. M. Harrison, D. Lin, Evidence for early (> 44 Ma) Himalayan crustal thickening, Tethyan Himalaya, southeastern Tibet. *Earth Planet. Sci. Lett.* **274**, 14–23 (2008).
95. Z.-C. Liu, F.-Y. Wu, Z.-L. Qiu, J.-G. Wang, X.-C. Liu, W.-Q. Ji, C.-Z. Liu, Leucogranite geochronological constraints on the termination of the South Tibetan Detachment in eastern Himalaya. *Tectonophysics* **721**, 106–122 (2017).
96. H. Chen, Z. Tian, B. Tuller-Ross, R. L. Korotev, K. Wang, High-precision potassium isotopic analysis by MC-ICP-MS: An inter-laboratory comparison and refined K atomic weight. *J. Anal. At. Spectrom* **34**, 160–171 (2019).

Acknowledgments: We are grateful to G. Bergantz for valuable discussions, two anonymous reviewers for insightful comments and suggestions, and C.-T. Lee for the efficient editorial handling. **Funding:** This work is supported by the National Key R&D Program of China (2019YFA0708400) and the National Natural Science Foundation of China (grant no. 42121002). **Author contributions:** Z.-Z.W. and F.-Z.T. conceived the project. F.-Y.W., Z.-C.L., and X.-C.L. collected samples. Z.-Z.W. performed K isotope analysis. Z.-Z.W. finished the original draft under the supervision of F.-Z.T. All authors reviewed and edited the manuscript. **Competing interests:** The authors declare that they have no competing interests. **Data and materials availability:** All data needed to evaluate the conclusions in the paper are present in the paper and/or the Supplementary Materials.

Submitted 9 May 2022
Accepted 4 October 2022
Published 25 November 2022
10.1126/sciadv.abo4492